UNIVERSITY OF CALIFORNIA
RIVERSIDE

Processing of Transparent Rare Earth Doped Zirconia for High Temperature Light Emission Applications.

A Dissertation submitted in partial satisfaction
of the requirements for the degree of

Doctor of Philosophy

in

Mechanical Engineering

by

Corey Lee Hardin

March 2015

Dissertation Committee:
Dr. Javier Garay, Chairperson
Dr. Reza Abbaschian
Dr. Lorenzo Mangolini

The Dissertation of Corey Lee Hardin is approved:

_____

_____

_____

Committee Chairperson

University of California, Riverside

Dedications

This dissertation is dedicated to my wife Bethany and my 3 children Jacob, Noah, and Ethan. Without your love and support this would not have been possible.

ABSTRACT OF THE DISSERTATION

Processing of Transparent Rare Earth Doped Zirconia
for High Temperature Light Emission Applications.

by

Corey Lee Hardin

Doctor of Philosophy, Graduate Program in Mechanical Engineering
University of California, Riverside, March 2015
Dr. Javier Garay, Chairperson

The high fracture toughness of stabilized zirconia makes it one of the most widely applicable high temperature structural materials. However, it is not typicality considered for optical applications since the microstructure achieved by traditional processing makes it opaque. The aim of this dissertation is to develop processing methods for introducing new functionalities of light transparency and light emission (photoluminescence) and to understand the nanostructure-property relationships that make these functionalities possible. A processing study of rare-earth (RE) doped Zirconium Oxide (ZrO_2, zirconia) via Current Activated Pressure Assisted Densification (CAPAD) is presented. The role of processing temperature and dopant concentration on the crystal structure, microstructure and properties of the RE: ZrO_2 is studied. Microstructural analysis shows sub-100 nm grain size and homogeneous dopant distribution. X-ray diffraction and Raman analysis show that with increased dopant concentration the material changes from monoclinic to tetragonal. Structural analysis shows the material shows high hardness and toughness values 30% greater than similarly processed yttria-stabilized zirconia. Despite birefringence in the tetragonal phase, the samples are both highly transparent and photo-luminescent. Special

attention is paid to analyzing structural and photoluminescence development during densification, as well as the role of oxygen vacancies on the optical properties of the densified material. This material is shown to be a promising candidate for a number of applications including luminescence thermometry and high temperature light emission.

Table of Contents

List of Figures

List of Equations

1. Introduction

1.1 Motivation

The industry of photonics is becoming more and more important every year, and its success is tied to the continued development of the materials that are used. With markets in a number of industries such as the medical field, where lasers are becoming more and more important, the defense sector avionics, and telecommunication optical networking, there is a great demand for next generation photonic materials to drive innovation and application. The photonics industry market size was 438 billion dollars in 2011 and is expected to grow to 770 billion dollars by 2020 [1].

Sue to their high transparency, most materials used in the photonics industry are either single crystals or glasses. Some of the more prevalent single crystals include Nd:YAG (laser host), Ce: YAG (white LED phosphor), lithium niobate (electro-optic), and potassium dihydrogen phosphate (frequency doubling). These materials are extremely useful, but often expensive to produce and difficult to control. Glasses are a cheaper alternative, but often have inferior properties to single crystals.

Polycrystalline materials (commonly referred to as “ceramics” in the photonics industry) are an exciting alternative to single crystals. There has been considerable worldwide interest in polycrystalline ceramics for optical applications since Akio Ikesue and coworkers produced the first polycrystalline ceramic Nd:YAG sample with the same slope efficiency as single crystal Nd:YAG. [2]

Polycrystalline ceramics have a number of advantages over single crystals. They can be produced in near net shapes, thereby eliminating costly machining and increasing the range of applications for materials. Companies such as Surmet Corporation are producing net shaped polycrystalline ceramics for applications such as transparent armor as well as radomes for missiles which are difficult to machine from single crystals. There are also new levels of microstructural control available. By controlling the layering of starting powders in a polycrystalline ceramic green body, very complex structures can be produced that would be very difficult to produce with single crystals [3]. For example, the dopant concentration across a laser crystal can be controlled in order to homogenize thermal load from optical pumping [3]. It has also been shown that polycrystalline ceramics can achieve higher levels of dopant concentration than can be achieved in single crystals[4], [5]. These advantages among others make optical polycrystalline ceramics a very exciting field.

The goal of this is dissertation is to develop processing methods for producing non-cubic (birefringent) nanocrystalline ceramics with high visible transparency and photoluminescent properties. Current activated pressure assisted densification is used to achieve the high levels of microstructural control needed. In this work, a new functionality of luminescence thermometry is added to an already impressive material, zirconium oxide (zirconia). Microstructural control allows us to stabilize the tetragonal phase to enhance structural properties while also limiting grain and pore sizes to make the material transparent, despite the birefringence of the tetragonal structure. This allows for production of a high strength, transparent, functionally doped luminescent polycrystalline ceramic

material with a wide variety of applications, especially for high temperature luminescence applications.

The structure of this work is as follows. Chapter 1 outlines the introduction and motivation, chapter 2 discusses processing of conventional yttria-stabilized zirconia, chapter 3 presents densification and characterization of Tb:ZrO_2, and finally chapter 4 discusses conclusions and future work. In section 1.2 an overview of the benefits of nanocrystalline structure is presented. In section 1.3, the theory of the structure and properties of zirconium oxide is discussed. The final section of the introduction, section 1.4 will introduce the background of terbium doped zirconium oxide. The main body of work is presented in Chapter 2, where the processing and characterization of Tb:ZrO_2 is presented. In Section 2.1, the experimental procedure for producing Tb:ZrO_2 is presented. Methods for microstructural and mechanical characterization are presented in section 2.2, followed by optical characterization methods in section 2.3. Section 2.4 presents the results and discussion for Tb:ZrO_2. Material structure was analyzed utilizing x-ray diffraction, Raman spectroscopy, and scanning electron microscopy, while mechanical properties were measured via Vickers indentation. Optical characterization of Tb:ZrO_2 includes inline transmission, photoluminescence, and luminescence lifetime. Section 3.5 investigates the relationship between microstructure during densification and the development of photoluminescence properties in Tb:ZrO_2.

1.2 Current Activated Pressure Assisted Densification and the Benefits of Nanocrystalline Structure

There are a number of different methods that can be utilized to produce polycrystalline ceramic materials. Some of the most common methods are free sintering, hot pressing, and hot isostatic pressing (HIP). Free sintering is the simplest process where powder is pressed into a green body then placed in a conventional furnace and fired. Hot pressing and hot isostatic pressing process the green body under pressure (uniaxial pressure for hot pressing, isostatic pressure for HIP) inside a vacuum chamber. The green body in these units can be heated with conventional heating elements or with induction heaters. The limitation of these methods is that processing is very slow, with times on the order of hours to days in order to produce a dense polycrystalline ceramic body. These long processing times at high temperatures lead to large amounts of grain growth and limit processing to "equilibrium" phases.

A solution to this problem is Current Activated Pressure Assisted Densification (CAPAD, also known by its trade name SPS). Figure 1 shows a schematic of the CAPAD apparatus. In CAPAD, powder is first loaded into a graphite die and plunger system, then inserted into a vacuum chamber between two electrodes. The system can apply high uniaxial pressure through these electrodes of up to 140 MPa in a traditional configuration and up to 1 GPa in high pressure configurations. A high current is then applied to the sample (up to 6000A) to heat the sample via joule heating at rates often >300^{o}C/min, leading to a typical experiment lasting less than 15 minutes.

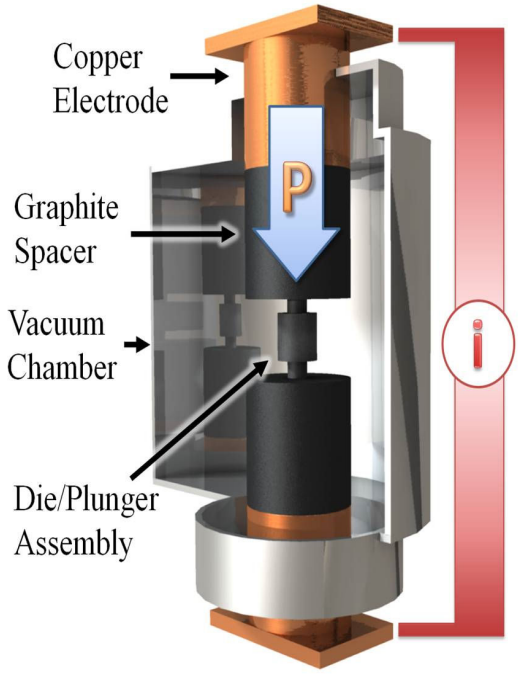

Figure 1: Schematic of CAPAD Apparatus (Schematic Courtesy of Dr. Jason Morales)

CAPAD allows for a number of benefits in the final polycrystalline ceramic body. The reduced exposure time of the sample to high temperatures leads to a significant drop in grain growth, allowing nanostructure from powders to be retained in dense bulk polycrystalline ceramics. This reduced time also allows for stabilization of meta-stable phases and structures that cannot be produced utilizing conventional methods. It also allows for higher doping levels of polycrystalline ceramics[5], which has applications in number of materials systems including optical and semiconductor materials. The combination of high heating rate, high pressure, and high current also leads to a significant reduction of the processing temperature required to densify a polycrystalline ceramic. This allows for a further reduction in grain growth, making CAPAD a very powerful tool for producing nanocrystalline polycrystalline ceramics. This also allows greater flexibility in

processing. Higher density can be achieved at the same temperature, which opens the door for processing of materials that would usually decompose or change phase at the temperature normally needed to densify.

Nanocrystalline materials have a number of benefits over their coarse-grained counterparts. From a mechanical properties perspective, by reducing grain size you can achieve higher yield strength and an increase in hardness. The performance of a thermoelectric material can be improved by decreasing grain size as this leads to a decrease in thermal conductivity. Magnetic materials can be enhanced by combining hard and soft magnetic materials into nanocomposites with enhanced magnetic properties[6].

There are a number of benefits for optical materials as well. Defects in a material such as pores and grain boundaries (in birefringent materials) can lead to scattering in a material, thereby diminishing optical performance. The presence of these defects can be detrimental, but the strength of their effects is related to the dimension of the defect.

The degree of transmission loss caused by pores can be reduced be decreasing the pore dimension. Mie scattering theory gives the transmission loss due to pores in a material by the following equation[7]:

$$T = \exp\left\{-\frac{3}{\frac{2tQ_{sca}(r,\lambda)}{d_{pore}(N)}}\right\}$$

Equation 1: Scattering Caused by Pores from Mie Theory

Where d is the diameter of pores, t is the sample thickness, N is the quantity of pores in the sample, and Q_{sca} is the efficiency factor for scattering. From modeling performed by

Klimke et. al[7] in yttria-stabilized zirconia, the transmission loss can be reduced from ~75% to ~5% by simply changing the pore diameter from 400nm to 50nm (pore concentration = 0.02%.) By utilizing nanocrystalline powder and proper CAPAD processing, the pore diameter of a polycrystalline ceramics can be greatly reduced, therefore enhancing the transmission of the polycrystalline ceramic even at equivalent pore volume concentrations.

In materials with an isotropic refractive index grain boundaries do not act as scattering sites and therefore grain size is not as critical. In anisotropic crystal systems where the refractive index is not the same in all directions scattering occurs due to birefringence. Figure 2 shows a schematic of the differences in optical scattering mechanisms between isotropic and anisotropic materials. In these materials systems it becomes critical to reduce the grain size to at least ~1/2 the wavelength of light in order to reduce scattering effects.

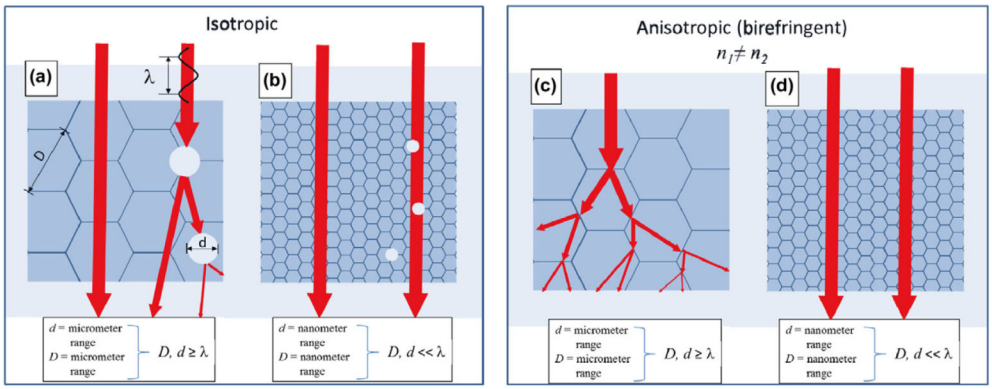

Figure 2: Optical Scattering Mechanisms in Isotropic and Anisotropic Materials [8]

There are a number of different models for analyzing scattering losses caused by birefringence. The most accurate is Mie theory, however this method is very intensive and

therefore not as practical as other methods such as the Rayleigh Gans Debye (RGD) approximation or the Rayleigh approximation.

The RGD approximation is extremely useful as it directly relates inline transmission to grain size and birefringence. The inline transmission of a material is given by the following equation:

$$T_I = (1 - R_s)\exp\left(-\frac{3\pi^2 r \Delta n_{ave}^2 t}{\lambda_0^2}\right), \qquad R = \frac{1-2n}{n^2+1}$$

Equation 2: RGD Approximation

Where Δn_{ave} is the average birefringence, r is the grain radius, λ is the wavelength of light, and R is reflection loss. This method is extremely convenient and has been shown to be an excellent model for many nanocrystalline optical materials, especially Aluminum Oxide. It has been shown to deviate slightly in materials systems with high levels of birefringence and nanoscale grains such as nanocrystalline tetragonal zirconia[7]. For these cases the Rayleigh approximation has been shown to be more accurate. The inline transmission from the Rayleigh approximation is given by the following equation[7]:

$$T_{IT} = (1 - R)\exp\left\{\left(-\frac{128\pi^4 r^3}{18\lambda^4}\right)\left[\frac{\Delta n_{ave}(2n + \Delta n_{ave})}{2}\right]^2 t\right\}$$

Equation 3: The Rayleigh Approximation

Where Δn_{ave} is the average birefringence, r is the grain radius, λ is the wavelength of light, and R is reflection loss.

In both of these equations it becomes clear that in order to achieve high levels of transparency in a birefringent material, it is necessary to minimize the grain size. Figure 3

shows the relationship between in-line transmission and grain size for alumina samples produced by a number of different groups.

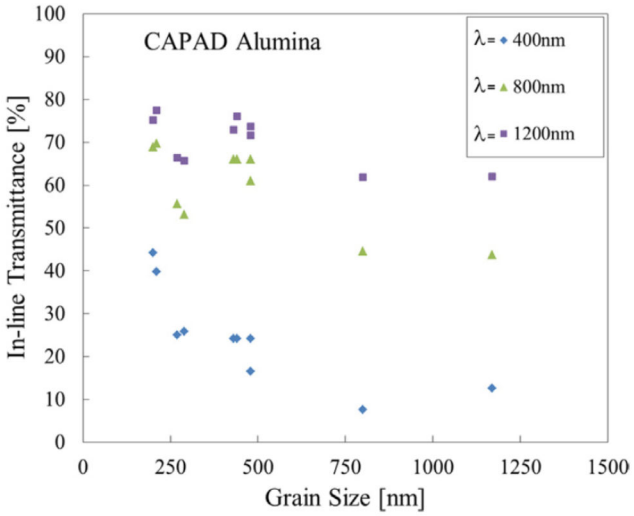

Figure 3: In-line Transmission vs. Grain Size for CAPAD Alumina Produced in Various Studies [8]

The in-line transmission of the material is greatly increased at lower grain sizes, especially at lower wavelengths. Transmission of 400nm light is increased from ~10% at 800nm grain size to almost 50% at 200nm grain size.

1.3 Structure and properties of Zirconium Oxide

There are 3 main structures of ZrO_2: Cubic, Monoclinic, and Tetragonal. All 3 are closely related to the cubic fluorite structure (Caf_2). The lowest temperature phase is monoclinic, which is typically stable below 1000 ^oC. The tetragonal phase becomes stable as a transition phase from 1000 ^oC up to 2300 ^oC where the cubic phase becomes stable. The cubic and tetragonal phases are typically stabilized by doping with oxides such as

MgO, CaO, Y_2O_3, Sc_2O_3, Er_2O_3, or Al_2O_3. The stabilization mechanism of these phases is generally accepted as due to the creation of oxygen vacancies associated with this doping. The basic mechanism is still unproven, but modeling suggests that the stabilization of tetragonal and monoclinic phases are controlled by structural disorder around the oxygen vacancies, rather than by the substitutional dopant cations [9].

The coordination number of the dopant is important in the degree of stabilization caused by the dopant. The lower the coordination number of the cation the more oxygen vacancies are generated. Cations used to stabilize zirconia can have a coordination number of 8, 7, or 6 depending on the number of oxygen vacancies associated with each cation substitution. A cation with a coordination number of 8 will generate no vacancies, 7 will generate 12.5% oxygen vacancies, and a coordination number of 6 will generate 25% oxygen vacancies. Full stabilization occurs when ~50% of the Zr^{4+} ions become seven coordinated, which means ~5-6% oxygen vacancies [10]. The two most common stabilizing dopants are CaO and Y_2O_3. Full cubic stabilization occurs with a CaO content of 12-22%, and with an Y_2O_3 content of ~16-75%.[10]

There are 3 different oxygen vacancy structures in Zirconia. One where an isolated oxygen vacancy interacts with 4 Zr atoms as its nearest neighbors, one where the vacancy interacts with a single Y doping atom and 3 Zr atom nearest neighbors, and finally one where the vacancy interacts with two separate Y doping atoms and 2 Zr atom nearest neighbors. Figure 4 shows a schematic of the 3 different vacancy structures in Yttria-stabilized Zirconia.

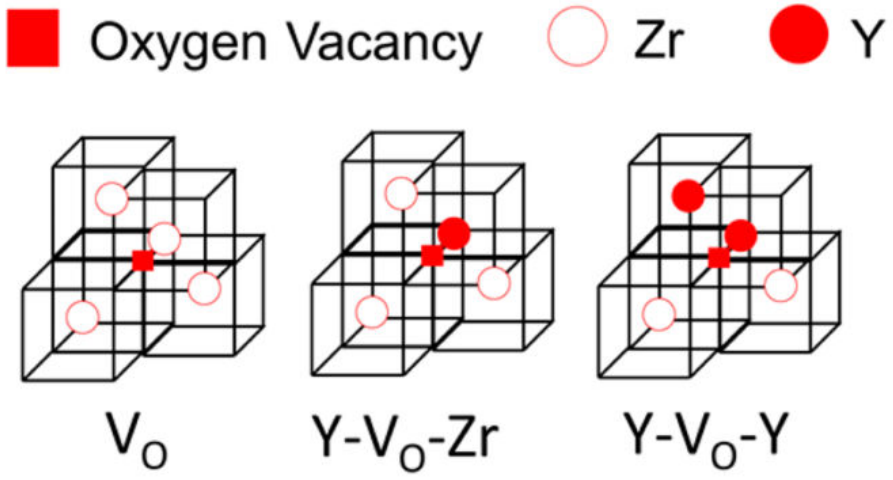

Figure 4: Oxygen Vacancy Defect Structure in Yttria-Stabilized Zirconia [11]

In general the Y-VO-Y has been shown to be the most stable defect structure, although this is not universally accepted [12], [13]. At high levels of dopant more complicated defect configurations can occur, such as the interaction between two of these doping units (~12.5% Y), and the interaction between two doping unit pairs (~25%).

Tetragonal zirconia polycrystalline ceramics are of considerable interest due to their variety of desirable properties including high strength, which can exceed 1GPa, fracture toughness greater than 15 MPa $m^{1/2}$, excellent wear properties, and thermal expansion coefficients close to that of iron [14]. The main factor in the strength of tetragonal zirconia polycrystalline ceramics is the diffusionless martensitic transformation from tetragonal phase to monoclinic phase that occurs under applied stress.

1.4 Background for Terbium Doped Zirconia

Stabilized zirconium oxide (zirconia) is one of the most technologically important

and widely used structural ceramics due to its excellent thermal stability, low thermal conductivity (important for thermal barrier applications) [15] and high fracture toughness. Despite its widespread use, polycrystalline zirconia is not usually thought of as a material suitable for optical applications because it is usually opaque. Some recent studies however, showed that with careful control of the microstructure, zirconia can be reliably made transparent [16], [17] yielding a versatile optical-structural ceramic.

Luminescent functionalization of polycrystalline ceramics through rare earth (RE) doping has also attracted considerable attention lately. There is interest in RE-doped polycrystalline ceramics for solid state lighting [18], laser host materials [5] and for luminescence thermometry [19]. The latter application is particularly interesting for zirconia, since partially stabilized zirconia is common in high temperature structural applications such as protective coatings in jet turbine engines[19]. Luminescence thermometry takes advantage of the temperature dependent photoluminescence of rare earth ions to measure the temperature of the ceramic part. One of the major advantages in that it is sensitive to does not require contact which makes it possible to assess temperature of moving parts.

Successful demonstrations of luminescent RE doping of zirconia have been presented by different groups[20]–[23]. In these studies, the approach was to add a small amount of luminescent RE (Ho, Er, Sm, etc.) as well as yttrium—the RE serves for the luminescence functionality while Y is for stabilizing the tetragonal phase. These studies confirm that luminescence provides a valuable integrated measurement scheme in zirconia. Tb is an ideal luminescence thermometry material for a number of reasons. First, Tb^{3+}

displays excellent photoluminescence in the blue-green spectrum where signal to noise ratio over thermal radiation is higher. Figure 5 shows photoluminescence spectra of three popular luminescence thermometry dopants in an Y_2SiO_5 host as compiled by Chambers and Clarke [19].

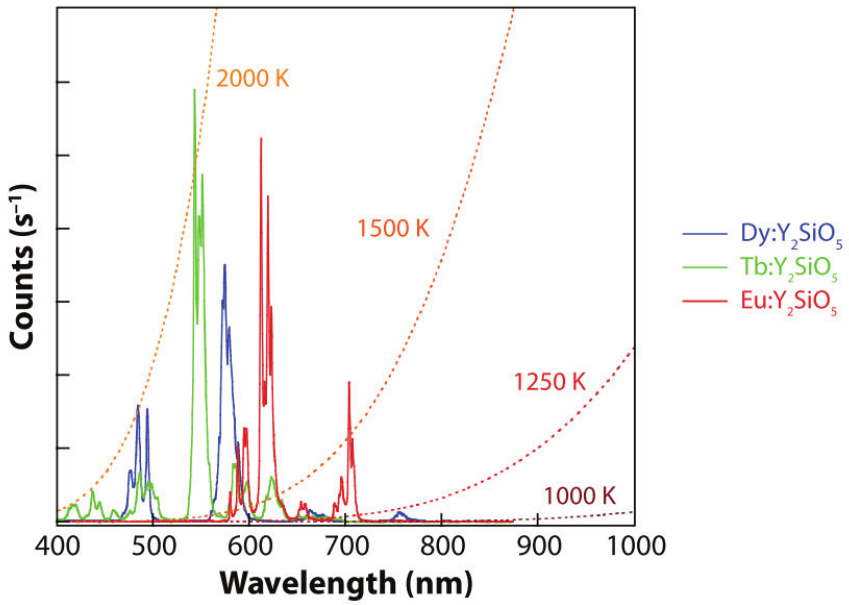

Figure 5: Photoluminescence Spectra of Various Luminescence Thermometry Dopants in an Y_2SiO_5 Host. Dashed Lines Represent Radiation Background at Various Temperatures. [19]

From this it can be seen that the 543nm luminescence peak of Tb has the highest signal-to-noise ratio of the three dopants at high temperatures, with signal above background radiation levels even as high as 2000 K.

Furthermore, if we look at the equation for temperature dependence of luminescence lifetime, Tb shows excellent promise. Equation 4 shows the relation between measured photoluminescence lifetime and temperature [22], [24].

$$\tau(T)^{-1} = \tau_R^{-1} + \left(\tau_{MPR}^{0} \left[1 + \left(\exp\left(\frac{h\omega}{kT} - 1 \right)^{-1} \right) \right]^{-\frac{\Delta E}{h\omega}} \right)^{-1}$$

Equation 4: Dependence of Photoluminescence Lifetime on Temperature

Where τ is the measured photoluminescence lifetime, τ_r is the temperature independent component of luminescence lifetime, τ_{MPR}^{0} is the multi-phonon relaxation rate at low temperature, ω is the phonon wavelength, and ΔE is the energy gap between the ground state and excited state. The multi-phonon relaxation rate depends on the phonon modes that are available in the host material, while the energy gap is dopant dependent. Therefore by comparing the energy gap of different dopants, we can gain insight into the potential for long high temperature luminescence lifetime. One of the highest temperature luminescence thermometry dopants is Eu^{3+} with an energy gap of 1.51 eV and typical maximum operating temperatures of 1000-1200 ^{o}C for luminescence thermometry[19]. Tb^{3+} has an energy gap of 1.82 eV, 20% higher than that of Eu^{3+} doping, and has been shown to be useful up to at least 1250^{o}C in a $GdAlO_3$ host[22]. Figure 6 shows a plot of lifetime vs. temperature for a number of luminescence thermometry materials as composed by Chambers and Clarke [19].

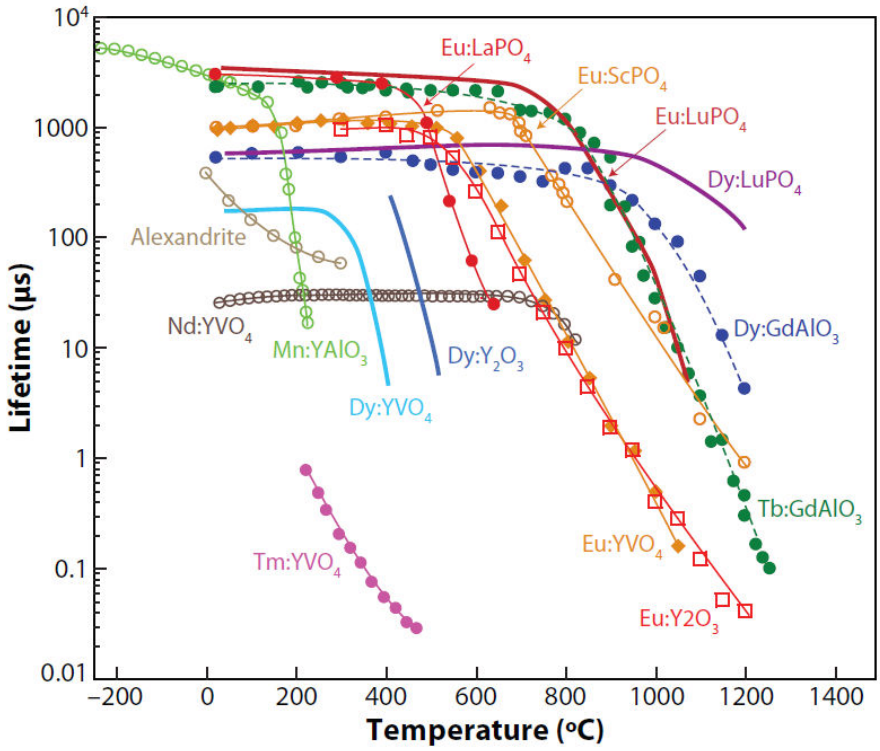

Figure 6: Lifetime vs. Temperature for a Number of Luminescence Thermometry Materials [19]

Previous attempts to produce Tb doped luminescent polycrystalline zirconia were unsuccessful [22], likely because of the formation of Tb4+ rather than Tb3+ which is the ion that luminesces under the desired conditions.

Utilizing current activated pressure assisted densification (CAPAD) we can stabilize meta-stable phases that cannot be produced utilizing conventional processes. Although CAPAD has used recently to produce a wide variety of transparent ceramics, most of the work has been done on cubic (optically isotropic) polycrystalline ceramics that do not luminesce [8].

Material	Optical Symmetry	Demonstrated Functionality
MgO	Isotropic	Passive
$MgAl_2O_4$ (Spinel)	Isotropic	Passive
YAG	Isotropic	Passive
Cubic-YSZ	Isotropic	Passive
Y_2O_3	Isotropic	Passive
Lu_2O_3	Isotropic	Passive
α-Al_2O_3	Birefringent	Passive
Dy_2O_3	Isotropic	Faraday Effect
Nd:YAG	Isotropic	Passive
Ce:YAG	Isotropic	Passive. . Visibla
Tb:AlN	Birefringent	Visible Luminescence
Tb:ZrO_2 (this work)	Birefringent	Visible Luminescence

Table 1: List of Optical Materials Produced Via CAPAD

Here we present a method for producing tetragonal zirconia polycrystalline ceramics with good transparency that also luminesces in the visible. We used CAPAD to simultaneously react and densify zirconia and terbia powders. In contrast to previous work we use only one rare earth additive, Tb (rather than a combination of RE and Y) that serves to both stabilize the zirconia and provide visible luminescence. Furthermore we concentered on producing tetragonal zirconia since it has superior mechanical properties compared to cubic zirconia.

2. Tb: ZrO2 Densification and Characterization

2.1 Experimental Procedure

Commercially pure non-doped ZrO_2 (Tosoh Corporation), Tb4O7 (NanoAmor, 99.995 % purity, 46-60 nm size), Y2O3 (Inframat Advanced Materials, 99.95% purity, 30-50nm) were used to make the reaction-densified polycrystalline ceramics. We also prepared ceramics using pre-doped yttria powder (Tosoh Corporation TZ-3Y-E, ~50nm grain size). Each powder was weighed to generate the appropriate stoichiometry. The powders were then mixed manually using a mortar and pestle to obtain macro scale mixing of the powders. The powder was then mixed in a low energy ball mill in a glass jar using a 20:1 ball to powder ratio of 5 mm ZrO_2 grinding balls.

The powder was then mixed manually in the mortar pestle again in order to break down any agglomerates formed in the low energy ball mill. Dopant levels were chosen in order to study the effects of the dopant both on the structural stabilization of the zirconia as well as the effects on optical and luminescent properties. The mixed powder was loaded into a graphite die between two 19 mm graphite punches and processed using our CAPAD apparatus.

The chamber was then evacuated to a pressure of 3×10^{-2} Torr. Then the sample was pre- pressed at a pressure of 70 MPa for 1 minute to break down agglomerates and make a more dense green body. The sample was then simultaneously heated to an intermediate temperature of ~550 ^{o}C and loaded to a pressure of 104 MPa over a 3 minute period. At this point the sample was heated at 200 ^{o}C/min to the desired processing

temperature and held to a total experiment time of 15 minutes at which point the current and load were released.

2.2 Microstructural and Mechanical Characterization

The as-produced samples were removed from the die and mechanically polished to uniform thickness. Density of samples were measured via Archimedes method utilizing a Mettler-Toledo XS104 scale with density measurement accessory. Samples were then analyzed using a Philips XL30-FEG SEM using both secondary electron (SE) and back-scattered electron (BSE) detectors to ensure phase uniformity. Pieces of the sample were broken off for fracture surface SE analysis to determine average grain size of the samples. Samples were characterized using a Bruker D8 powder XRD as well as a Horibia LabRam micro-Raman for phase analysis. Samples were mechanically tested using a Wilson Tukon 2100 hardness tester using a Vickers indenter. Hardness values were measured using 2 kg and fracture toughness was measured using a 5 kg load. Fracture toughness, KIC values were calculated using both the Niihara [13] and Anstis [14] equations.

2.3 Optical Characterization

The optical transmission of the samples were measured using a CARY 50 UV/VIS spectrometer. Steady state photoluminescence properties were measured using a Horiba Spex Fluorolog spectrophotometer. Photoluminescence decay measurements were made using the fourth harmonic of an ND:YAG laser (266 nm wavelength) and an Oriel

Instruments Cornerstone 260 ¼ meter monochromator with an Oriel 77341 photomultiplier tube.

2.4 Results and Discussion

Figure 7a shows sample density vs. processing temperature for Tb:ZrO_2 samples with 3% Tb while Figure 7b shows the effect of varying Tb dopant concentration while holding the processing temperature constant at 1150 ^oC.

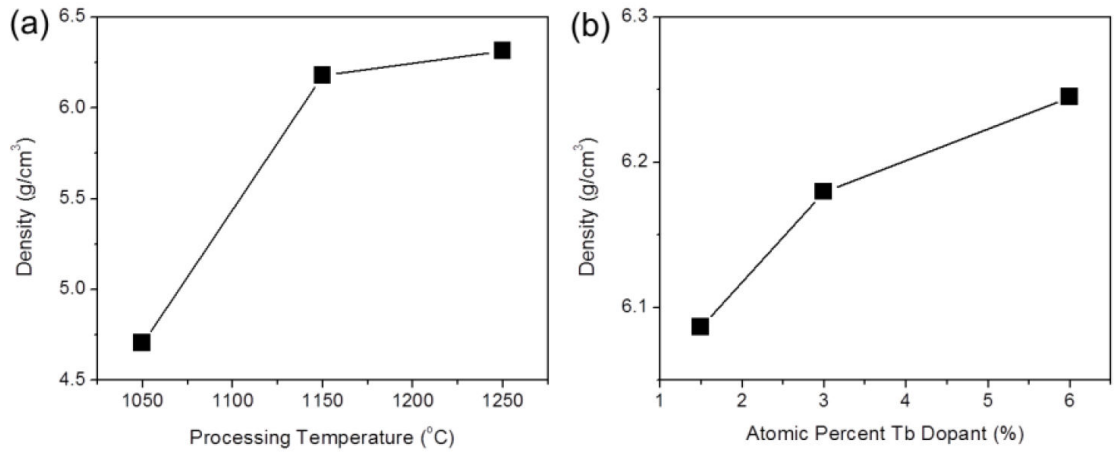

Figure 7: The effect of (a) processing temperature and (b) Tb dopant concentration on the bulk density of Tb:ZrO_2. A fixed Tb concentration (3%Tb:ZrO_2) was used for all sample in (a) and constant processing temperature of 1150° C was used in (b) (lines between points are guide to eye only)

As expected, the density of samples increases with processing temperature, because of higher densification (less porosity). The density of the samples is similar at temperatures above 1150^{o}C. The amount of Tb dopant also plays a role; the density increases with higher Tb content. This trend of increasing density is opposite to what is seen with yttria stabilization. R. P. Ingel et al.[25] studied the effect of Y_2O_3 concentration on the density

of YSZ. They report that the measured and calculated density of the YSZ decreases as the Y_2O_3 content is increased. For example, the calculated polycrystalline densities of YSZ were 6.16, 6.12 and 6.02 g/cm^3 when the concentrations of doped Y_2O_3 were 0, 1.5 and 6%, respectively. This dependence is caused by the increase in the charge compensating vacancies generated due to the different valence states of Zr^{4+} and Y^{3+}. This incorporation of Y_2O_3 into ZrO_2 causing the formation of vacancies for charge compensation can be written in Kroger-Vink notation as:

$$Y_2O_3 \rightarrow 2Y'_{Zr} + 3O_O^x + V_{\ddot{O}}$$

Equation 5: Kroger-Vink Notation for Y_2O_3 incorporation into ZrO_2

By contrast Tb can be Tb3+ or Tb4+ as indicated by the Tb_4O_7 stoichiometry. However, the doping of Tb which in Tb_4O_7 is effectively half Tb^{3+} and Tb^{4+} would still require charge compensation. One possibility is:

$$Tb_4O_7 \rightarrow 2TB'_{Zr} + 2Tb_{Zr}^x + 7O_O^x + V_{\ddot{O}}$$

Equation 6: Possible Kroger-Vink Notation for Tb_4O_7 incorporation into ZrO_2

Thus it is not likely that lack of vacancy formation is responsible for the increase in density with increasing Tb content observed in Figure 1 b. Instead the differing trend is likely due to the difference in atomic mass of Tb and Y. Increasing dopant concentration into ZrO_2 effects not only the lattice parameter and the crystal structure but also the overall molar mass. The relative atomic mass of Y is 88.91, compared to Tb which is 158.93 and about 1.8 times that of Zr (91.22). This effect of the mass difference could be responsible for the Tb content dependence that we observe being opposite to traditionally observed for Y. Although we cannot calculate the relative density or porosity concentration due to the lack of information of the theoretical density of Tb stabilized zirconia, the porosity of the

samples should be very small as evidenced by high transparency of the samples as will be discussed below.

Figure 8 are pictures of a 6% Tb: ZrO_2 ceramic placed on printed text on a light table. Figure 8a shows the as-processed sample while Figure 8b is the same sample after annealing in air at 700 ºC for 24 hours. Comparison of the pictures reveals that annealing in air changes the color of the sample; this effect will be discussed in detail below. The text is legible through the sample, confirming the high densities and transparency of our samples.

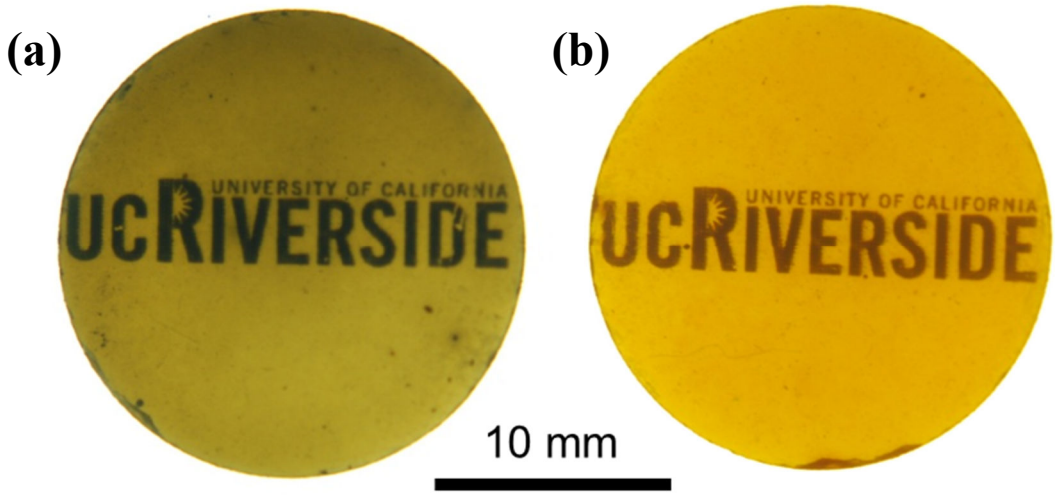

Figure 8: Photographs of a 6%Tb:ZrO_2 sample on the top of backlit text, demonstrating transparency. (a) as-processed sample. (b) sample annealed at 700° C for 24 hrs

It is well known that depending on the degree of stabilizing dopant (often Ca or Y) zirconia can be monoclinic, tetragonal or cubic. Figure 9 shows XRD (a) and Raman (b) spectra for zirconia samples produced with varying atomic percent Tb. For comparison, we also plotted Raman spectra for a non-doped ZrO_2 and two Y doped samples. One Y: ZrO_2

was made using the identical reaction/densification process as the Tb: ZrO_2, while another was made using commercially available pre-doped powder; we refer to the samples as 3% Y: ZrO_2 (R/D) and 3% Y: ZrO_2 (Tosoh), respectively. The results reveal that as the dopant level is increased, the structure of the samples changes from a pure monoclinic structure, as shown in the undoped sample, to a purely tetragonal phase as shown in the 6% Tb: ZrO_2 sample. The 1.5% and 3% Tb: ZrO_2 samples contain both monoclinic and tetragonal phases. These results confirm that Tb can serve to stabilize the tetragonal phase in zirconia. The Raman spectra of the as reaction/densified 3% Y:ZrO_2 are very similar to the 3% Tb:ZrO_2, while peak at ~260 cm^{-1} is more asymmetric in the sample made with pre-reacted commercial powder. Since Tb and Y can both be trivalent, it is likely that the stabilization mechanism is similar to Y stabilization.

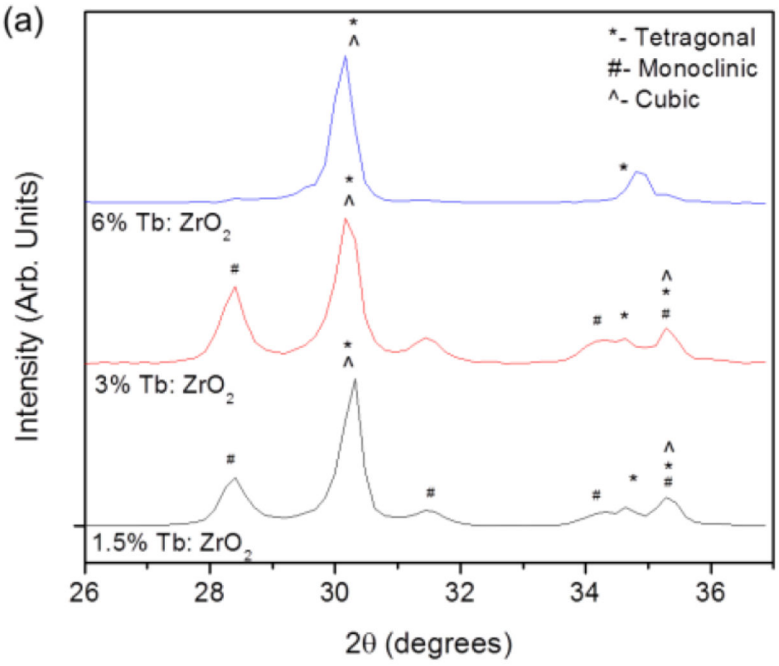

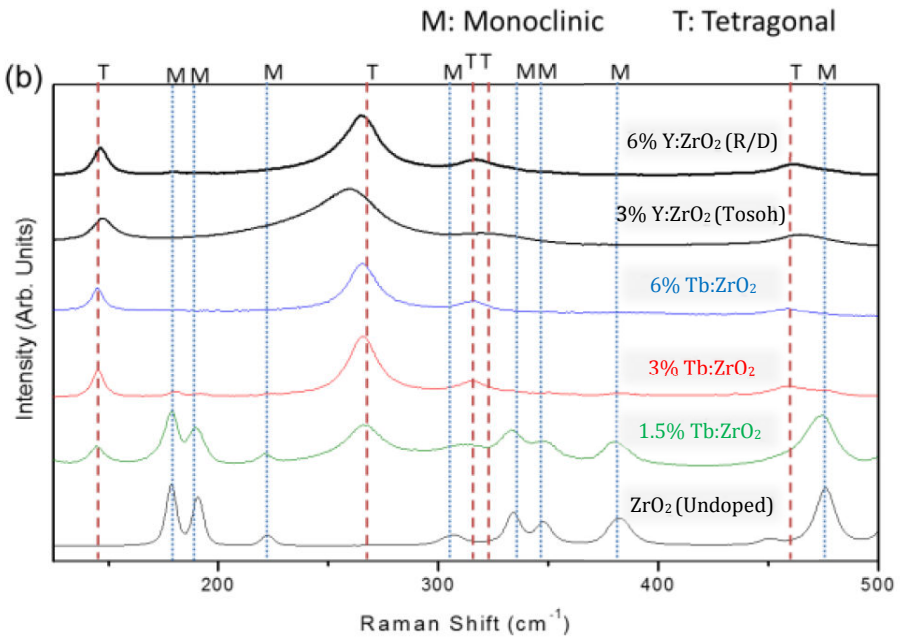

Figure 9: (a) X-ray diffraction profiles of Tb: ZrO_2 samples with varying Tb content and (b) Raman spectra of Tb: ZrO_2 samples with varying Tb content.

SEM micrographs of polished surfaces of Tb: ZrO_2 with varying atomic percent Tb using both secondary electron (SE) and back-scattered electron (BSE) detectors are shown in Figure 10. The micrographs show high phase uniformity and no dopant segregation. The lack of observable phase segregation suggests that the Tb ions have been incorporated into the ZrO_2 lattice, corroborating the Raman and XRD results which show that the Tb stabilizes the tetragonal phase.

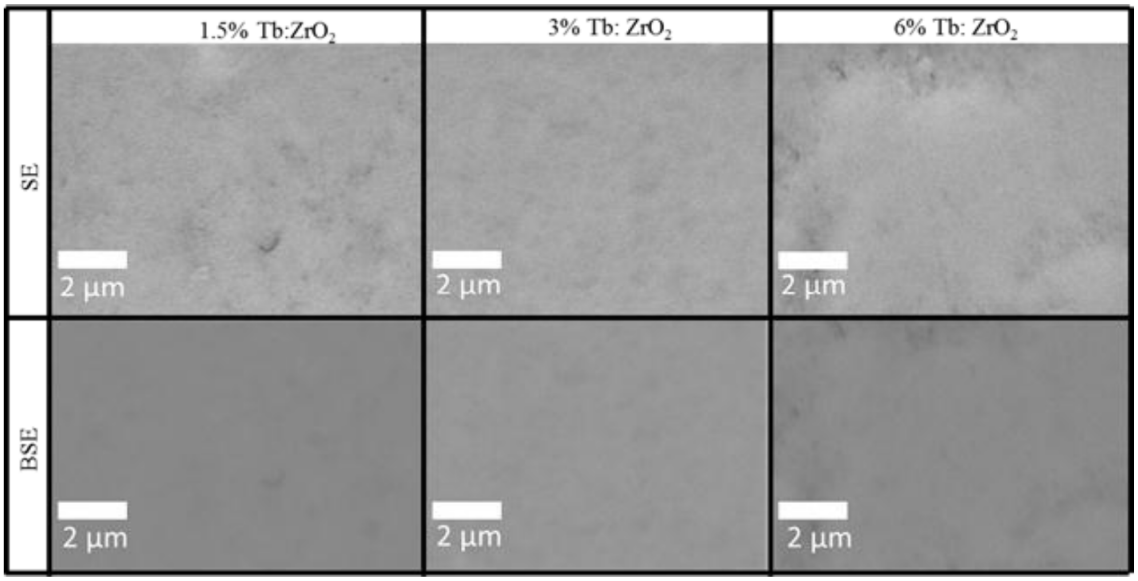

Figure 10: Secondary Electron (SE) and Backscatter Electron (BSE) Micrographs for Tb:ZrO2 samples with varying Tb content

Figure 11 shows SEM micrographs of fracture surfaces of the same samples shown in Figure 10, showing average grain sizes varying between 84 and 103nm. The fine grain sizes of the Tb: ZrO_2 samples produced by our reaction/densification method promise good optical and structural properties as will be discussed below.

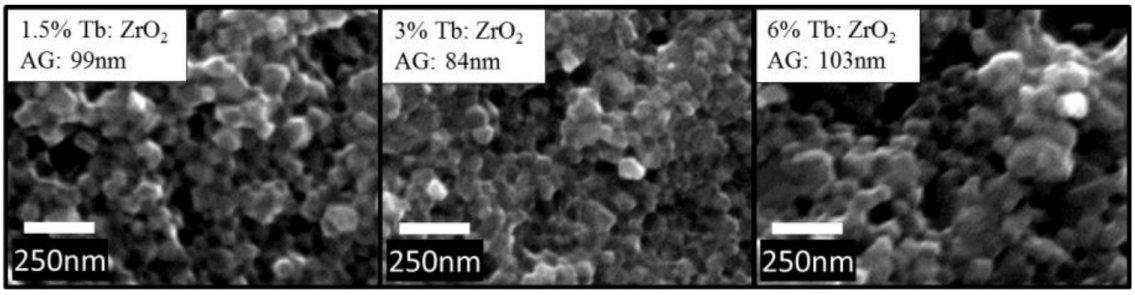

Figure 11: SEM of fracture surfaces of Tb:ZrO2 with varying dopant levels SEM

Figure 12 shows hardness and toughness measurements for both Tb and Y doped zirconia samples processed under identical conditions at 1150°C. The Tb: ZrO_2 ceramics

compare favorably with traditional yttria doped samples; the Y: ZrO_2 sample shows slightly higher hardness and slightly lower toughness values than same concentration Tb doped samples. The Hardness of Tb: ZrO_2 samples increases fairly linearly with dopant percentage. The fracture toughness ranges from 3.5 to almost 7 $MPa/m^{0.5}$ and is maximized at 3% Tb which is expected since at this concentration, the sample contains a mixture of tetragonal and monoclinic phases (see Figure 9). These are high fracture toughness values for a ceramic and confirm that Tb: ZrO_2 polycrystalline ceramics are suitable for structural applications.

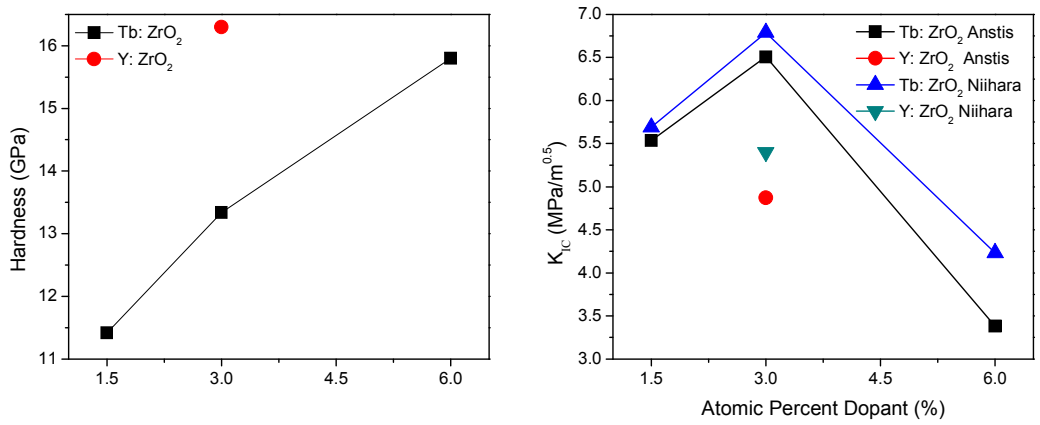

Figure 12: Hardness and Toughness of ZrO_2 vs. Dopant Level (Y or Tb). Lines between points are guide to eye only.

It has been shown that oxygen vacancies play an important role in the optical properties of YSZ [8], [16]. Specifically oxygen vacancies in zirconia have a positive charge so they can trap electrons, forming a color center that absorbs light in the visible. In Kroger-Vink notation an oxygen vacancy with a trapped electron can be written:

$$V_{\ddot{O}} + e' \rightarrow V_{\dot{O}}$$

Equation 7: Kroger-Vink notation for an Oxygen Vacancy with a Trapped Electron

We believe we observe a similar effect in Tb: ZrO_2. As seen in Figure 8, the color of our samples change significantly during annealing. In order to better understand this effect, we performed a series of experiments to determine the effects of annealing on the optical properties of Tb: ZrO_2. A 6% Tb: ZrO_2 was processed via CAPAD, polished, then annealed for up to 6 hours at 700 ^oC in a box furnace in air. The sample was polished and optical transmittance was measured. Figure 7a shows the effect of annealing in the presence of oxygen on the transmission for various anneal times and wavelengths. The transmission data was also used to calculate absorption coefficients using Beer's Law:

$$T = (1 - R)^2 e^{-\beta l}$$

Equation 8: Beer's Law

Where l is the sample thickness, T is transmittance, R for reflectance, and β is the absorption coefficient. The reflectance was calculated using the refractive index, n of YSZ (n = 2.2). These data are plotted vs. anneal time in Figure 13; the data reveal that the absorption coefficient decreases with annealing time for all wavelengths.

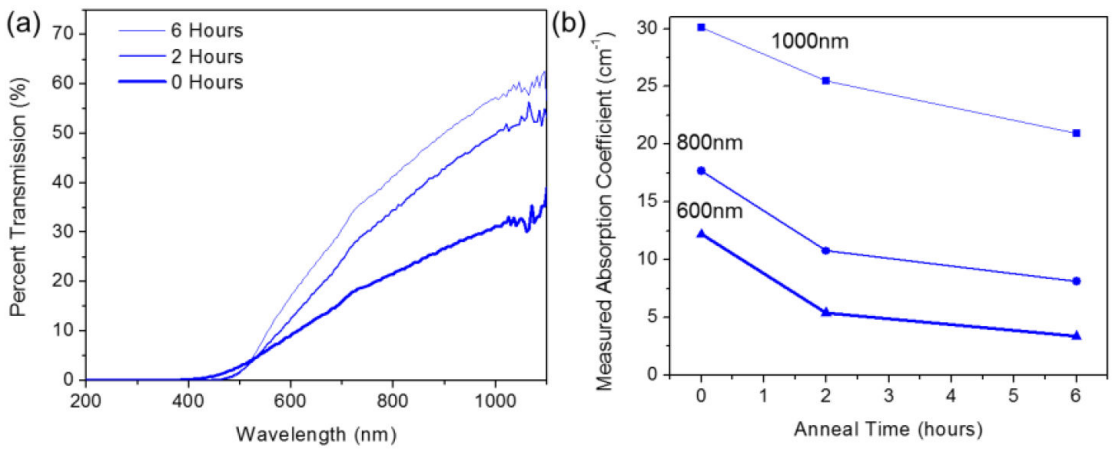

Figure 13: Effect of annealing on the (a) optical transmission and (b) absorption coefficients of 6% Tb:ZrO_2. (lines between points in (b) are guide to eye only)

It is likely that the decrease in β can be attributed to a decreased concentration of vacancies with trapped electrons, $[V_{\dot{O}}]$ as defined by Equation 1. Assuming a proportional relationship between absorption coefficient and vacancy concentration, we can write:

$$\beta \propto [V_{\dot{O}}]$$

Equation 9: Relationship between Absorption Coefficient and Vacancy Concentration

We can check the validity of the assumption that β is affected by vacancy concentration (and therefore oxygen diffusion) by applying an analytical diffusion model. Using Fick's second law for slab geometry with an initial vacancy concentration, $[V_{\dot{O}}]_0$ the time dependent average concentration of oxygen vacancies, $[V_{\dot{O}}]$ is given by:

$$[\overline{V_{\dot{O}}}](t) = \frac{1}{h}\int_0^h [V_{\dot{O}}](x,t)dx = \frac{8[V_{\dot{O}}]_0}{\pi^2}\sum_{j=0}^{\infty}\frac{1}{(2j+1)}\exp\left(-\left[\frac{(2j+1)\pi^2}{h}\right]Dt\right)$$

Equation 10: Solution to Fick's Second Law for a Slab Geometry

Where h is the thickness of the slab and D is the diffusion coefficient. A good approximation to Equation 10 is:

$$\frac{[\overline{V_{\dot{O}}}]}{[V_{\dot{O}}]_0} = \frac{8}{\pi^2}\exp\left(-\frac{t}{\tau}\right)$$

Equation 11: Approximation of Fick's Second Law

Where the relaxation time τ is

$$\tau = \frac{h^2}{\pi^2 D}$$

Equation 12: Relaxation time, τ, in Approximation Fick's Second Law

The relaxation time is a function of the diffusivity, D of the diffusing species; the higher the diffusivity the shorter the relaxation time. Figure 14 is a plot of the natural log of normalized absorption coefficient vs. anneal time. Absorption coefficients for each wavelength were normalized to the corresponding maximum value for each wavelength. The dashed lines are fits of the experimental points. The R^2 values of the fits are shown in the inset for each of the wavelength. They range from 0.98 for 600 nm light to 0.89 for light in the near-IR (1000 nm). This good fit suggests that the absorption coefficients decay exponentially as in Equation 11. Also plotted in Figure 14 is a curve calculated using previously measured oxygen volume diffusivity [26] at the same temperature (700 ºC), i.e. by using D from the literature directly into Equation 11Equation 12. The slopes of the lines in Figure 14 (corresponding to 1/τ) are quite similar. The measured values for τ at various wavelengths are reported in the inset along with calculated values using oxygen diffusion. At all wavelengths the measured τ is close to τ calculated for oxygen diffusion (within a

factor of 2). By contrast, the corresponding time constants calculated using carbon diffusivity in zirconia [27] and zirconium volume diffusivity in zirconia [28] are 1×10^{13} and 2.5×10^{13} respectively—13 orders of magnitude higher than our measured time constants. These data strongly suggest that the observed effect of annealing time on β of Tb: ZrO_2 is related to the average oxygen vacancy concentration, $[\overline{V_{\dot{O}}}]$ changing as oxygen diffuses back into the oxygen deficient ceramics.

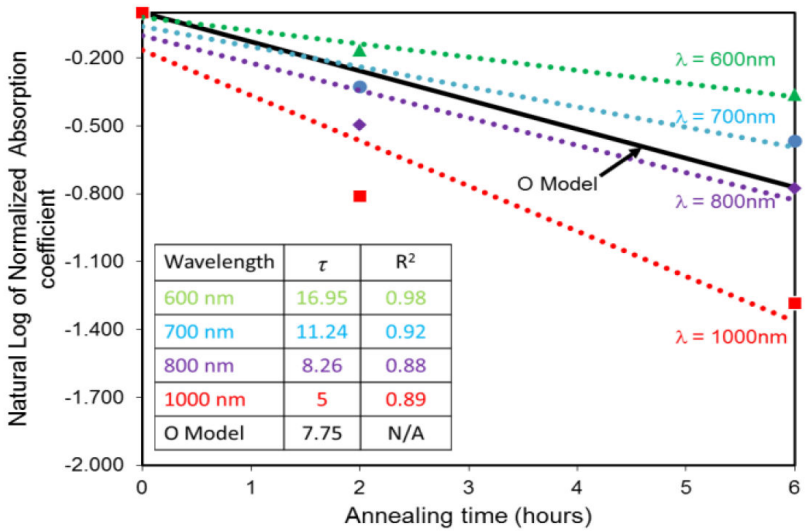

Figure 14: Measured absorption coefficients for Tb:ZrO_2 compared to Oxygen diffusion model. The inset tabulates the relaxation time, t and R^2 (for fit to exponential) for various wavelengths.

Figure 15 shows optical transmission of samples vs. atomic percent Tb. Sample transmission increases greatly with atomic percent Tb. We observe a transmission of <5% at 1μm for a 1.5% Tb sample vs. >50% transmission at 1μm for 6% Tb: ZrO_2. It has been shown that light transmission increases with decreasing grain size in birefringent polycrystalline ceramics [7], [29]. However since the average grain size of our Tb: ZrO_2 is

similar at all Tb contents (Figure 11) it is not likely the differences in transparency as a function of Tb content we observe is caused by differing grain size. Instead we feel that the observed differences are caused by changes in relative birefringence. Klimke et al. surveyed available data on the birefringence (Δn) of tetragonal YSZ and showed that the apparent (Δn) can vary significantly between 0.2 to 0.9 [7]. It should be noted that these values even on the low end are higher than for hexagonal alumina (Δn = 0.008), making producing transparent tetragonal zirconia particularly difficult. The low transparency we observe at lower content is likely due to high birefringence caused by the existence of monoclinic and tetragonal zirconia (Figure 9). Klimke et al. [7] also provided calculations based on Mie theory that fit well with experimental data. A similar analysis is not possible for our samples since Mie scattering theory neglects absorption which is very important in our Tb: ZrO_2 samples as shown in Fig. 2 and 7. It is worth emphasizing that the optical transparency of the tetragonal 6%Tb: ZrO_2 is over 50% at 1μm. We attribute the high transparency of the 6%Tb: ZrO_2 samples to high density, small grain size and relatively low birefringence.

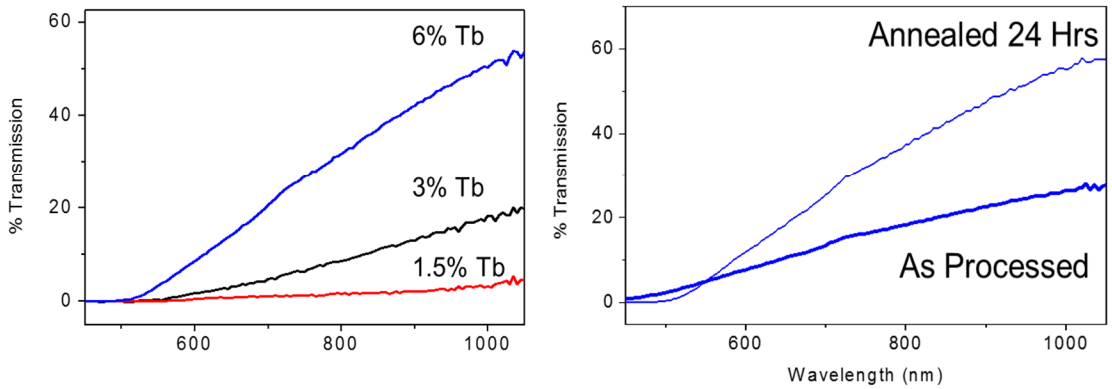

Figure 15: (a) Optical Transmission vs. Wavelength for Varying dopant content in Tb:ZrO_2 (b) Optical Transmission vs. Wavelength for a 6% Tb:ZrO_2 Sample As Processed and after a 24hr anneal at 700 ^oC

The luminescent properties of the Tb doped samples were also investigated. Figure 10 shows photoluminescence spectra for varying atomic percent Tb under 290 nm excitation. All three dopant levels show sharp luminescence peaks, with intensities that increase with Tb concentration. The peaks correspond to the Tb^{3+} transitions expected from the Dieke diagram [30]; the $^5D_4 \rightarrow {}^7F_6$ centered around 500 nm and the $^5D_4 \rightarrow {}^7F_5$ transition centered around 550 nm. As mentioned before, Tb ions are multivalent and can be Tb^{3+} or Tb^{4+}. The peaks in the luminescent spectra (Figure 16) confirm the existence of Tb^{3+} in Tb:ZrO_2 fabricated using the CAPAD method. It is worth emphasizing that previous attempts to produce luminescent Tb:ZrO_2 using conventional sintering did not succeed [22]. The lack of success was attributed to the formation of primarily Tb^{4+}.

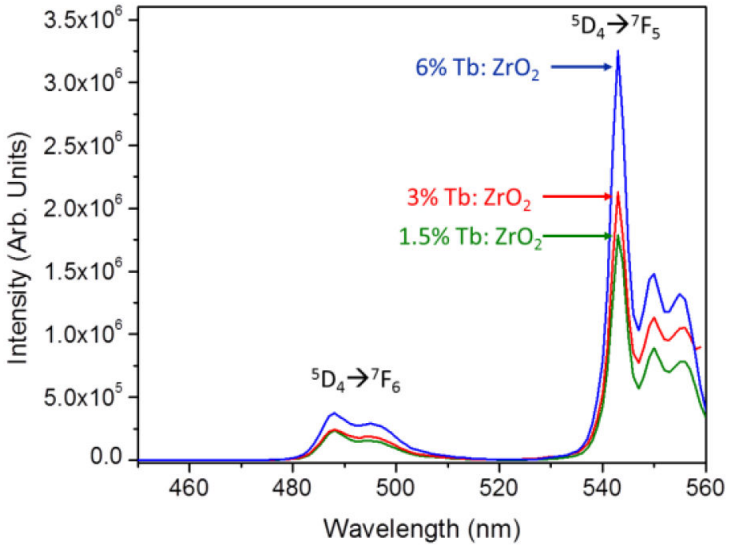

Figure 16: Photoluminescence Spectra vs. wavelength for varying atomic percent Tb in Tb:ZrO2 (290nm Excitation)

The amount of Tb concentration affected the luminescence decay as well (Figure 11a). The 1.5% Tb:ZrO_2 shows a significantly longer luminescence lifetime (1.11 ms) than the 3% (0.613 ms) and 6% (0.657ms) samples as seen in Figure 11b. This shorter lifetime is indicative of dopant quenching at higher levels of Tb doping. The temperature dependence of luminescence intensity is reported in Figure 12, which shows the change in luminesce spectra vs. temperature for measurement temperatures ranging from 23 ^{o}C to 200 ^{o}C. Detectable changes in luminescent intensity with temperature suggest that Tb:ZrO_2 can be used in temperature sensing applications. Although the lifetime of luminescence is known to be a more sensitive temperature probe than intensity [6] we do not have temperature dependent lifetime measurement at this time. However we expect the lifetimes to show temperature dependence and are currently investigating this possibility. [31]

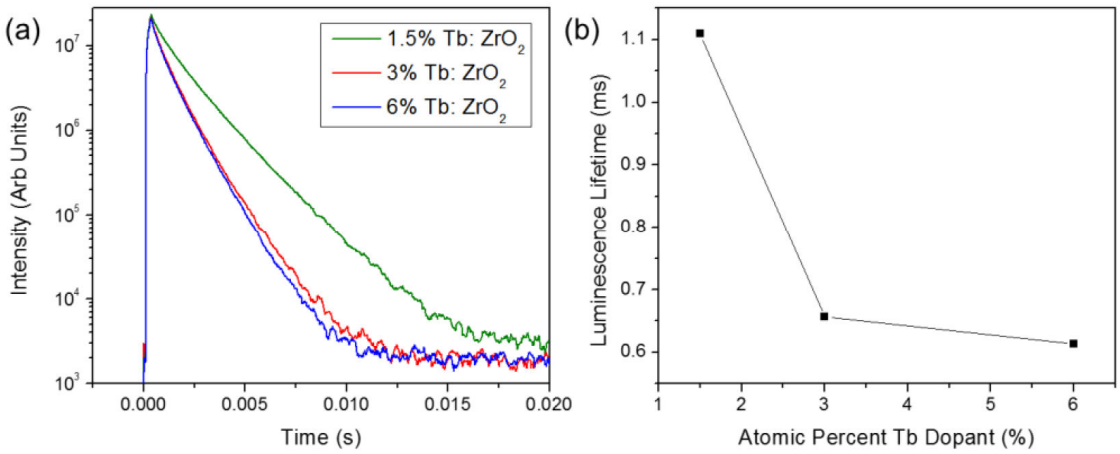

Figure 17: Photoluminescence Decay vs. Dopant Level (15 point moving average applied to (a) for clarity), lines between points in (b) are guide to eye only)

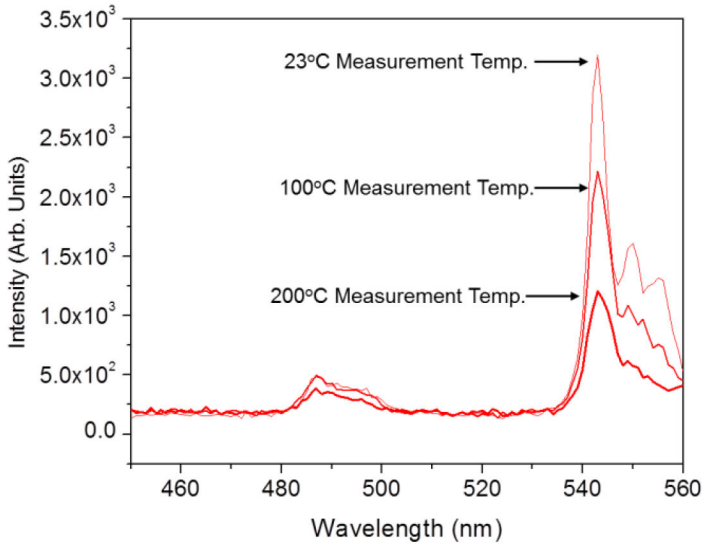

Figure 18: Effect of measurement temperature on photoluminescence intensity for 3% Tb:ZrO_2

2.5 Microstructure/Photoluminescence Development

In order to better understand the development of photoluminescence in this material, a series of experiments were performed to analyze the state of the material

throughout the densification process. 1.5 grams of 8% Tb: ZrO_2 mixed powder (as described previously) was processed at a heating rate of 300 ^oC/min from the start of the experiment. Simultaneously a compressive pressure of 104Mpa was applied over 3 minutes. The samples were heated to a series of different temperatures at which the process was stopped and the samples were cooled at ~300 ^oC/min in order to quench the structure at that point. The process was stopped at 5 different points. The first stop was at 1000 ^oC, which is just before the onset of densification. The second stop was at 1100 ^oC, which is approximately the onset of densification. The third stop was at 1150 ^oC and the fourth at 1200 ^oC, both of which are during the main densification event as the sample approaches and reaches final processing temperature. The final fifth stop represents a fully densified sample was held at 1200 ^oC for a total experiment time of 900s. Figure 19 shows a graph of the temperature and extension of the fully densified sample vs. time. The various stopping points are overlaid on the plot to demonstrate how the various stopping points correlate to the densification profiles.

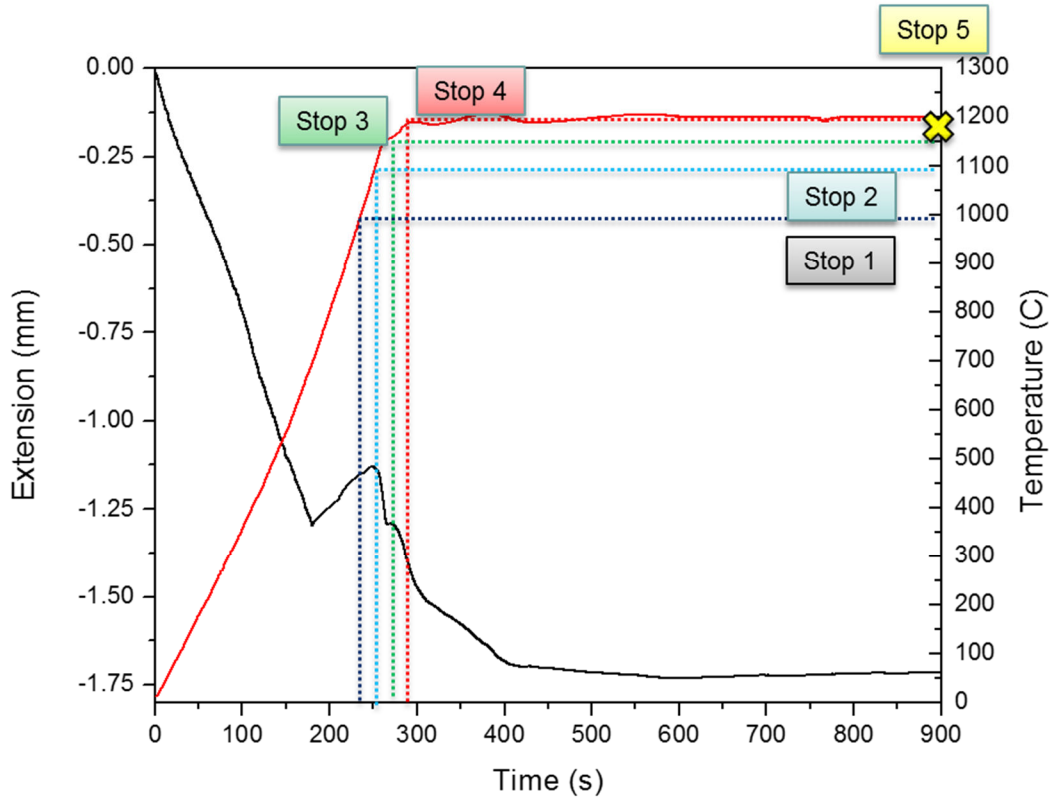

Figure 19: Schematic of microstructure/photoluminescence development study methodology

Processed samples were polished before further analysis was performed using an Allied High Tech Products MetPrep 3 grinder/ polisher with silicon carbide paper down to 1200 grit. Density measurements were performed utilizing Archimedes method in order to determine relative density vs. temperature during densification. Samples with densities below 80% were wrapped in Parafilm in order to avoid absorption of water into pores. Figure 20 shows the density vs. temperature for the various stops.

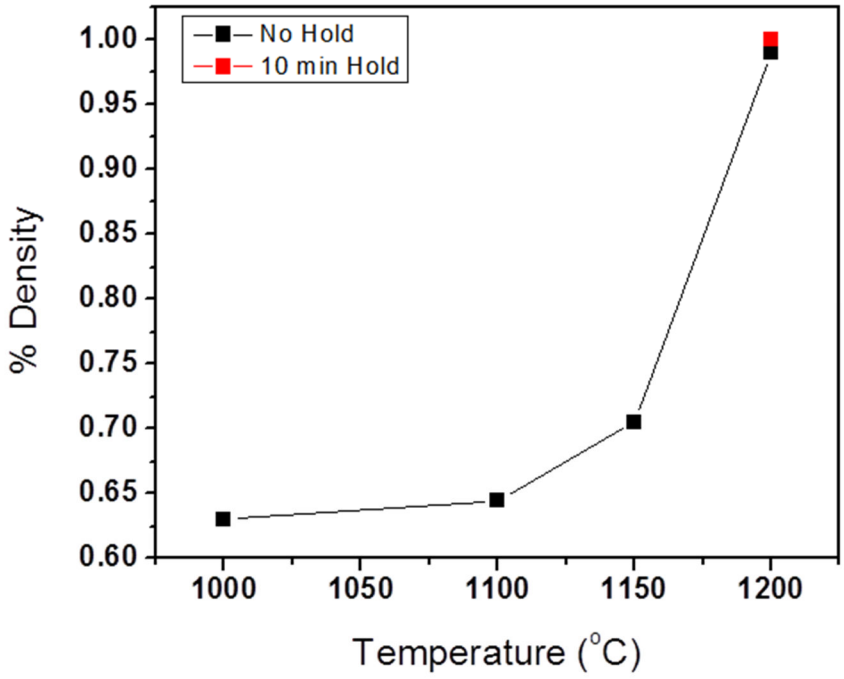

Figure 20: Relative density vs. temperature during densification of an 8% Tb:ZrO_2

As expected there is little difference between stop 1 at 1000 ºC, when densification hasn't begun, and stop 2 at 1100 ºC when it is just beginning, with a difference of ~2%. The density moderately increases to 70% by stop 3, at 1150 ºC. By 1200ºC the sample is 99% percent dense, with a slight increase to full density after holding at temperature.

Figure 21 shows Raman spectroscopy (a) and X-ray diffraction (XRD) analysis (b). Results show a starting mixture of monoclinic phase ZrO_2 and Tb_4O_7.This progresses towards a pure tetragonal phase by 1200ºC.

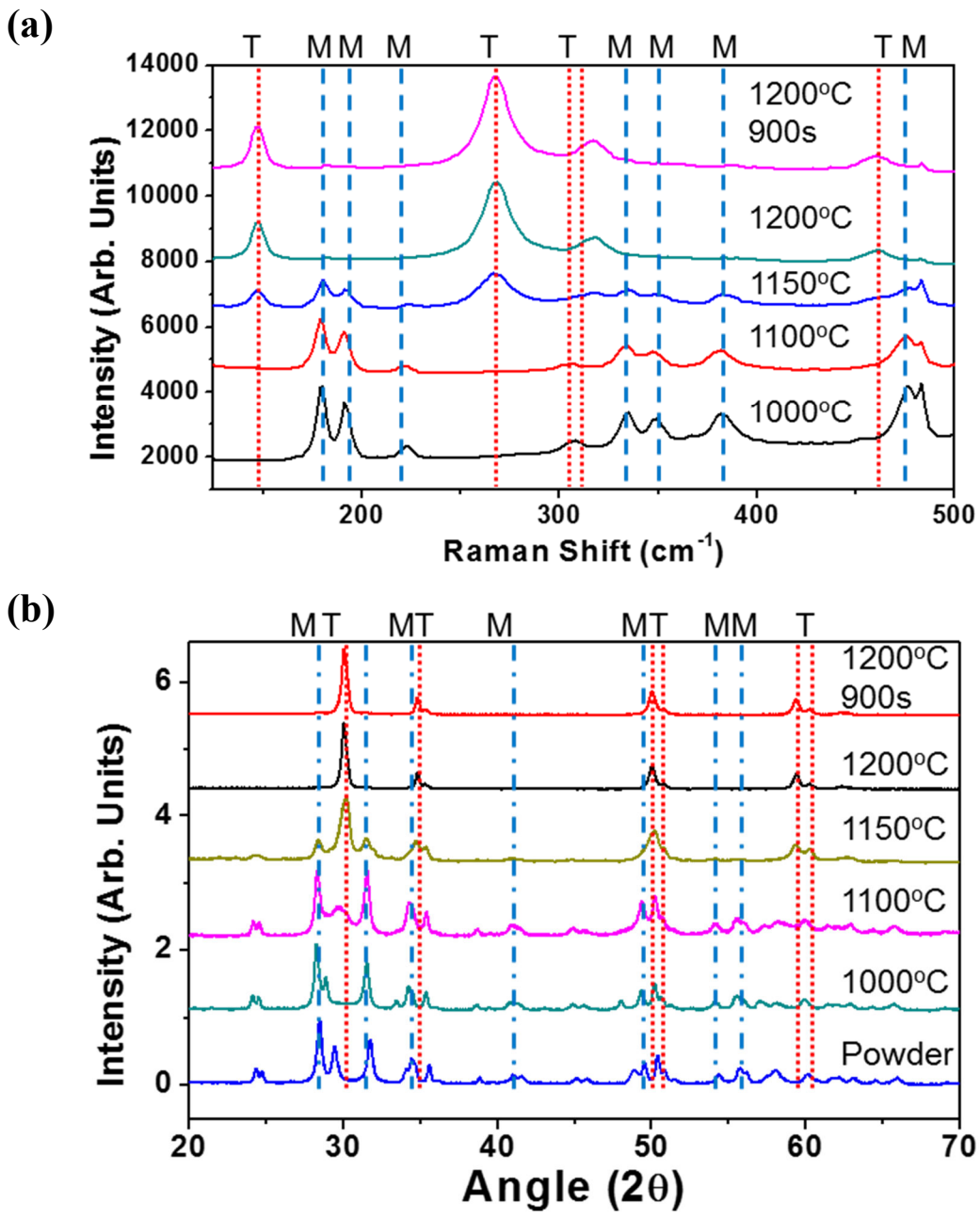

Figure 21: Phase progression of Tb: ZrO_2 as shown by (a) Raman Spectroscopy and (b) X-ray diffraction

Rietveld refinement was performed to analyze the relative phase composition utilizing Panalytical HighScore Plus software's Rietveld refinement package. Figure 22

shows a plot of relative mass percentage of Monoclinic and Tetragonal Zirconia, as well as cubic Tb_4O_7 (no other phases were detected.)

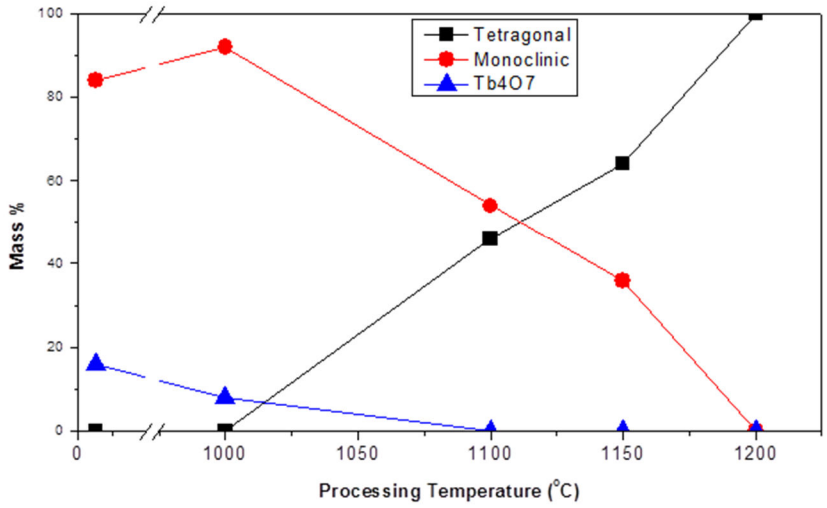

Figure 22: Phase Development During Densification of Tb:ZrO_2 as determined via Rietveld Refinement of XRD

This data shows a mix of ~84% monoclinic ZrO_2 and 18% cubic Tb_4O_7 in the starting powder. By 1000 °C Tb_4O_7 content has decreased slightly to ~10% as the Tb_4O_7 dissolves into the ZrO_2, with the rest of the sample remaining in the monoclinic phase. By 1100 °C all signs of the starting cubic Tb_4O_7 are gone and the transition from monoclinic to tetragonal phase has begun. At this point the sample is ~55% monoclinic and 45% tetragonal. The reaction continues at 1150 °C with tetragonal becoming the dominant phase at ~62% concentration. By the time the sample reaches 1200 °C the transformation is complete and the sample is purely tetragonal.

Rietveld results were corroborated using both XRD and Raman intensity ratios. Phase analysis can be determined in a Monoclinic/Tetragonal mixture via XRD by

analyzing the relative intensities of the tetragonal (111) plane and the monoclinic (111), $(11\bar{1})$ planes. Equation 13 shows the method for determining the ratio of tetragonal phase in such a system.

$$m_t\% = \frac{I_t(111)}{I_m(111) + I_t(111) + I_m(11\bar{1})}$$

Equation 13: Equation for Determining Ratio of Tetrgonal Phase from XRD Analysis [32], [33]

Equation 14 shows a very similar method of determining tetragonal phase utilizing Raman spectra. Peak intensities of the tetragonal peaks at 148 and 263 cm^{-1} and the monoclinic peaks at 182 and 191 cm^{-1} are analyzed. This equation includes an experimental correction factor as determined by Yang et. al. [34]

$$V_t\% = \frac{.97(I_t^{148} + I_t^{263})}{.97(I_t^{148} + I_t^{263}) + I_m^{182} + I_m^{191}} \times 100\%$$

Equation 14: Equation for Determining Ratio of Tetragonal Phase from Raman Spectra [34]

Figure 23 shows a comparison of the three analysis methods. All 3 methods show good agreement. Maximum deviation of 17% between XRD intensity and Rietveld occurs at 1100 ^oC where the (111) tetragonal peak is very broad and not fully developed as shown in Figure 22.

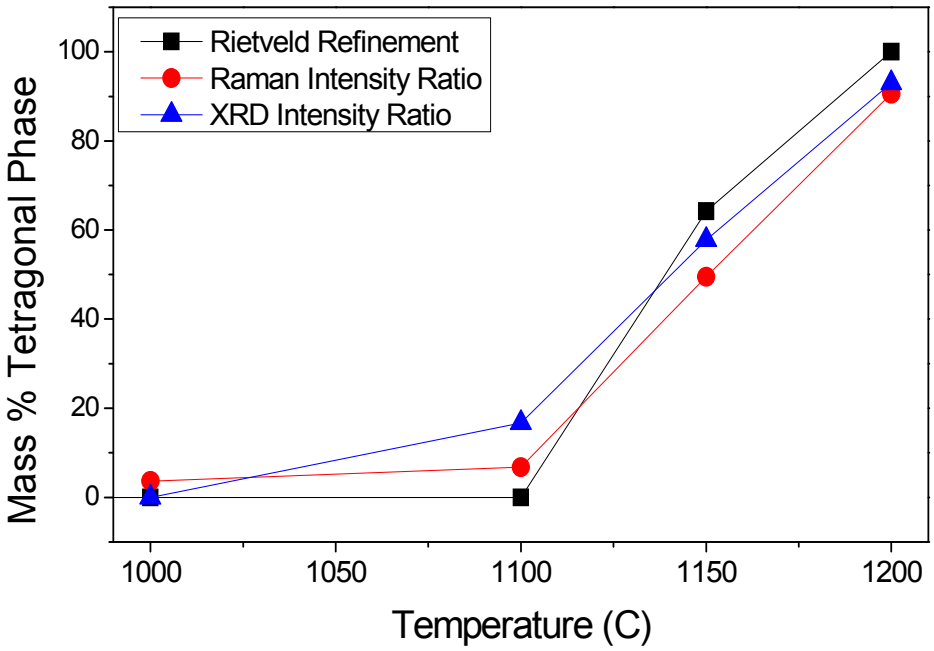

Figure 23: Comparison of calculated mass percentage of tetragonal phase as determined via Rietveld Refinement, XRD Intensity Ratio, and Raman Intensity Ratio Methods

SEM characterization was then performed, similar to Figure 10 and Figure 11. Secondary (SE) and backscatter (BSE) electron micrographs were acquired on polished surfaces in order to analyze phase homogeneity. Secondary electron micrographs of fracture surfaces were acquired to show microstructural development. Figure 24 shows these images.

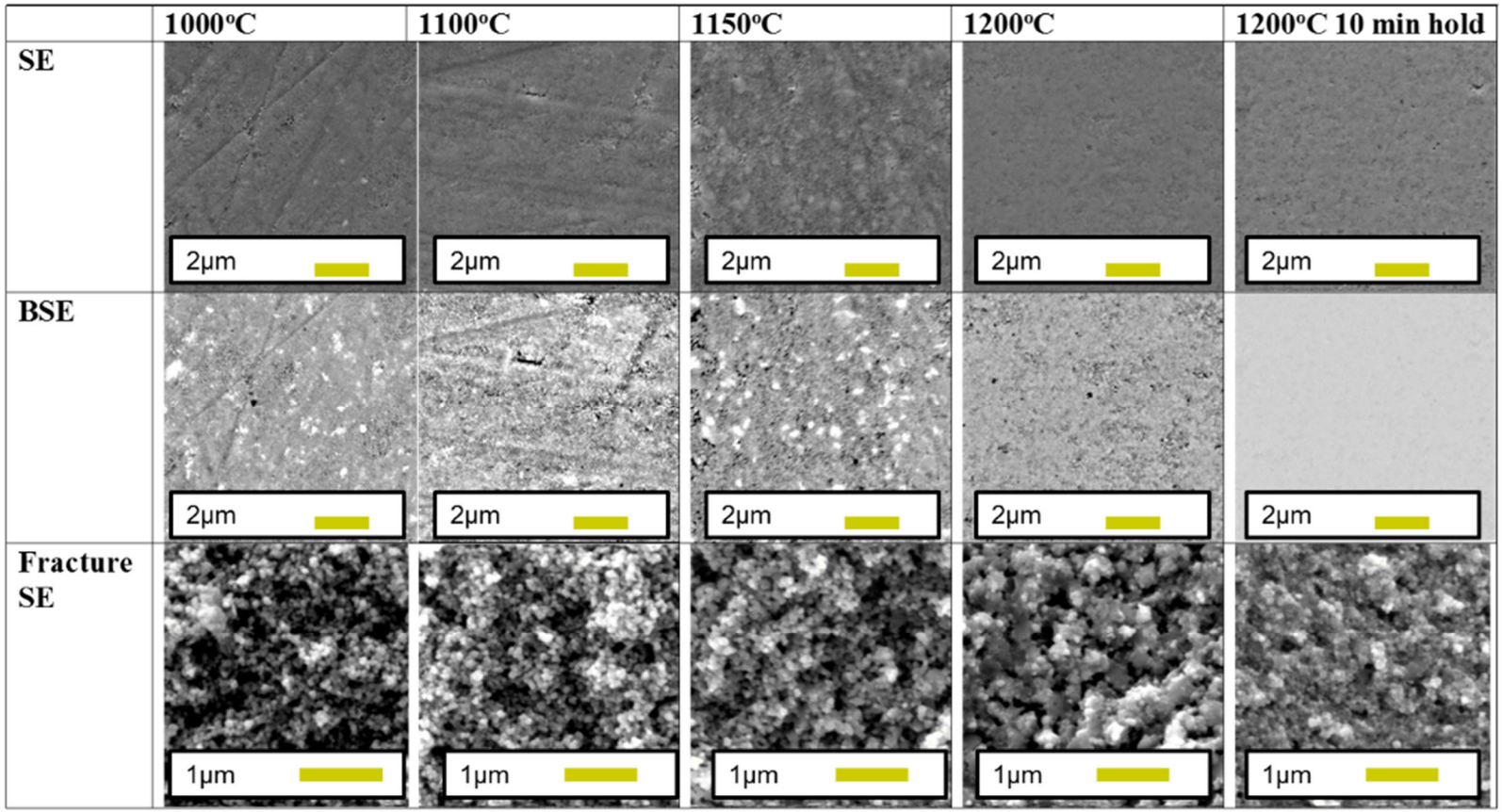

Figure 24: Secondary Electron (SE) and Backscatter Electron (BSE) Micrographs for Tb: ZrO_2 during densification

The fracture surface micrographs highlight one of the capabilities of the CAPAD process by showing that the grains only grow from the initial powder grain size of ~50nm to a final grain size of less than 100nm. This limited amount of grain growth (50nm) would be impossible in conventional methods without introducing some sort of grain pinning mechanism to limit grain growth. Secondary and backscatter electron images of polished surfaces show high levels of dopant segregation in samples processed below 1200 ^{o}C. A clear transition can be seen between the sample processed at 1150 ^{o}C, which shows many clusters of segregated Tb dopant, and the sample processed at 1200 ^{o}C which shows signs of porosity but no evidence of segregated dopant. After being held at 1200 ^{o}C for 10 minutes, this residual porosity is removed and a fully dense, slate gray backscatter image is observed indicating no dopant segregation.

Photoluminescence measurements were performed on each sample to investigate the relationship between photoluminescence and microstructural development. Figure 25 shows photoluminescence spectra for each sample, as well as the development of the maximum photoluminescence intensity during processing.

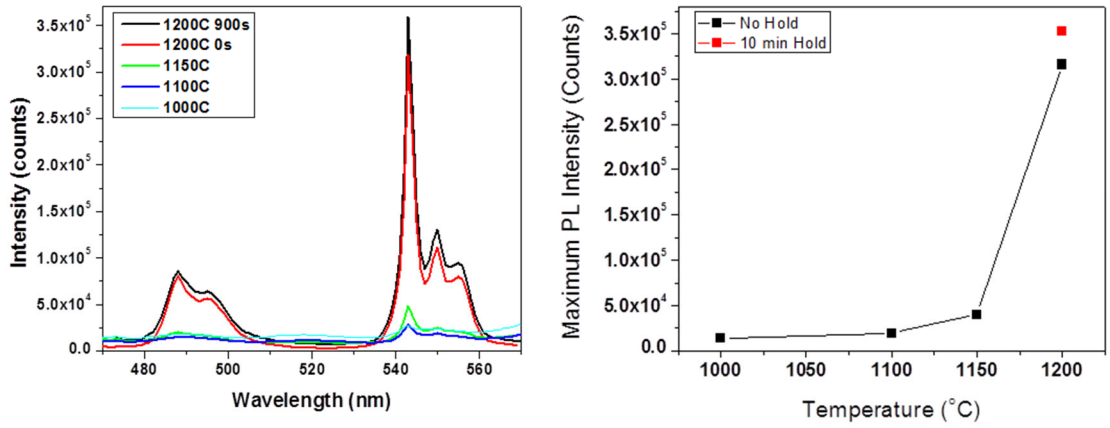

Figure 25: Development of photoluminescence during densification of Tb: ZrO_2

Photoluminescence shows an interesting correlation to microstructure. The normalized spectra of the luminescence remains unchanged under all conditions. This is due to the relatively insensitive nature of rare earth luminescence due to their protective outer electron shell. The intensity, however, changes greatly during densification. Intensity increases slightly from 1000 ºC to 1100 ºC, and again from 1100 ºC to 1150 ºC. The intensity is still fairly low at this point, as most of the dopant is clustered together and therefore experiences large amounts of concentration quenching. At 1200 ºC we see almost an order of magnitude increase in intensity from the 1150 ºC sample. This occurs as the Tb^{3+} dopant is integrated into the ZrO_2. As this occurs, the dopant is spread out homogenously, thereby limiting concentration quenching effects in the sample. There is another slight increase in intensity after the sample is held at 1200 ºC. This occurs due to the large increase in transparency of the sample, thereby increasing the activation volume of dopant and producing more photoluminescence intensity.

The drastic nature of the photoluminescence intensity over a relatively small temperature change from 1150 ºC to 1200 ºC is driven by the phase transition from monoclinic to tetragonal that occurs in this region. At 1150ºC the transition is beginning, but the sample is quenched before there is sufficient time for the dopant to be distributed. By 1200 ºC the phase transformation is complete. This transformation enhances densification and reaction rates significantly. A similar effect has been shown previously during reaction densification studies of YAG ceramics by Penilla et. al. [18] where it was demonstrated that utilizing CAPAD can enhance reaction rates by 2-3 orders of magnitude over those demonstrated in conventional processing.

3. Conclusions

Polycrystalline ceramics are an exciting alternative to single crystals for photonic applications. By utilizing CAPAD processing, nanostructured optical ceramics can be produced with novel structure and properties. We have presented a method for producing transparent, luminescent Tb: ZrO_2 ceramics using CAPAD. The ceramics have a high fracture toughness values and confirm that Tb: ZrO_2 ceramics could be used for structural applications. The optical transparency can be influenced by annealing in air and an analytical model of oxygen diffusion fits well with our experimental results suggesting that the absorption coefficient, β of Tb: ZrO_2 is related to the average oxygen vacancy concentration, $[\overline{V_{\dot{O}}}]$. The luminescent intensity and lifetime depend on Tb content. In addition the luminescent lifetimes are long and the luminescent intensity is influenced by temperature suggesting that the ceramics can be used in a wide range of applications such as temperature sensitive transparent armor, windows or thermal barriers. The fast kinetics of CAPAD were shown to induce very rapid dopant incorporation into the material, with the majority of dopant incorporation occurring within a narrow 50 ^{o}C window. This supports previous work that shows that CAPAD can be used to drastically enhance the reaction kinetics of materials.

4. Acknowledgements

Partial support of this work by the National Science Foundation (NSF Grant# DMR 0956071) is gratefully acknowledged. Some of the material in this thesis was previously published in the following papers:

1. Y. Kodera, C. L. Hardin, and J. E. Garay, "Transmitting, emitting and controlling light: Processing of transparent ceramics using current-activated pressure-assisted densification," *Scr. Mater.*, vol. 69, no. 2, pp. 149–154, Jul. 2013.

2. C. Hardin, Y. Kodera, S. Basun, D. Evand, and J. E. Garay, "Transparent, luminescent terbium doped zirconia: development of optical-structural ceramics with integrated temperature measurement functionalities," *Opt. Mater. ...*, vol. 39, pp. 1264–1269, 2013.

5. References

[1] B. Spectaris, VDMA, ZVEI, "Photonics Industry Report 2013," 2013.

[2] A. Ikesue and T. Kinoshita, "Fabrication and Optical Properties of High-Performance Polycrystalline Nd: YAG Ceramics for Solid-State Lasers," *J. Am. ...*, pp. 1033–1040, 1995.

[3] A. Ikesue and Y. Aung, "Ceramic laser materials," *Nat. Photonics*, pp. 721–727, 2008.

[4] E. H. Penilla, Y. Kodera, and J. E. Garay, "Simultaneous synthesis and densification of transparent, photoluminescent polycrystalline YAG by current activated pressure assisted densification (CAPAD)," *Mater. Sci. Eng. B*, vol. 177, no. 14, pp. 1178–1187, Aug. 2012.

[5] a. T. Wieg, Y. Kodera, Z. Wang, T. Imai, C. Dames, and J. E. Garay, "Visible photoluminescence in polycrystalline terbium doped aluminum nitride (Tb:AlN) ceramics with high thermal conductivity," *Appl. Phys. Lett.*, vol. 101, no. 11, p. 111903, 2012.

[6] J. R. Morales, S. Tanju, W. P. Beyermann, and J. E. Garay, "Exchange bias in large three dimensional iron oxide nanocomposites," *Appl. Phys. Lett.*, vol. 96, no. 1, p. 013102, 2010.

[7] J. Klimke, M. Trunec, and A. Krell, "Transparent Tetragonal Yttria-Stabilized Zirconia Ceramics: Influence of Scattering Caused by Birefringence," *J. Am. Ceram. Soc.*, vol. 94, no. 6, pp. 1850–1858, Jun. 2011.

[8] Y. Kodera, C. L. Hardin, and J. E. Garay, "Transmitting, emitting and controlling light: Processing of transparent ceramics using current-activated pressure-assisted densification," *Scr. Mater.*, vol. 69, no. 2, pp. 149–154, Jul. 2013.

[9] S. Fabris, A. T. Paxton, and M. W. Finnis, "A stabilization mechanism of zirconia based on oxygen vacancies only," vol. 50, pp. 5171–5178, 2002.

[10] S. Ho, "On the structural chemistry of zirconium oxide," *Mater. Sci. Eng.*, vol. 54, pp. 23–29, 1982.

[11] M. Boffelli, W. Zhu, and M. Back, "Oxygen Hole States in Zirconia Lattices: Quantitative Aspects of Their Cathodoluminescence Emission," *J. ...*, 2014.

[12] H. Ding, A. V. Virkar, and F. Liu, “Defect configuration and phase stability of cubic versus tetragonal yttria-stabilized zirconia,” *Solid State Ionics*, vol. 215, pp. 16–23, May 2012.

[13] a. Eichler, “Tetragonal Y-doped zirconia: Structure and ion conductivity,” *Phys. Rev. B*, vol. 64, no. 17, p. 174103, Oct. 2001.

[14] I. Nettleship and R. Stevens, “Tetragonal zirconia polycrystal (TZP)—A review,” *Int. J. High Technol. Ceram.*, vol. 3, no. 1, pp. 1–32, Jan. 1987.

[15] S. Ghosh, D. Teweldebrhan, J. R. Morales, J. E. Garay, and a. a. Balandin, “Thermal properties of the optically transparent pore-free nanostructured yttria-stabilized zirconia,” *J. Appl. Phys.*, vol. 106, no. 11, p. 113507, 2009.

[16] J. E. Alaniz, F. G. Perez-Gutierrez, G. Aguilar, and J. E. Garay, “Optical properties of transparent nanocrystalline yttria stabilized zirconia,” *Opt. Mater. (Amst).*, vol. 32, no. 1, pp. 62–68, Nov. 2009.

[17] S. R. Casolco, J. Xu, and J. E. Garay, “Transparent/translucent polycrystalline nanostructured yttria stabilized zirconia with varying colors,” *Scr. Mater.*, vol. 58, no. 6, pp. 516–519, Mar. 2008.

[18] E. H. Penilla, Y. Kodera, and J. E. Garay, “Simultaneous synthesis and densification of transparent, photoluminescent polycrystalline YAG by current activated pressure assisted densification (CAPAD),” *Mater. Sci. Eng. B*, Jun. 2012.

[19] M. D. Chambers and D. R. Clarke, “Doped Oxides for High-Temperature Luminescence and Lifetime Thermometry,” *Annu. Rev. Mater. Res.*, vol. 39, no. 1, pp. 325–359, Aug. 2009.

[20] M. M. Gentleman and D. R. Clarke, “Luminescence sensing of temperature in pyrochlore zirconate materials for thermal barrier coatings,” *Surf. Coatings Technol.*, vol. 200, no. 5–6, pp. 1264–1269, Nov. 2005.

[21] Y. Shen, M. D. Chambers, and D. R. Clarke, “Effects of dopants and excitation wavelength on the temperature sensing of Ln3+-doped 7YSZ,” *Surf. Coatings Technol.*, vol. 203, no. 5–7, pp. 456–460, Dec. 2008.

[22] M. D. Chambers and D. R. Clarke, “Terbium as an alternative for luminescence sensing of temperature of thermal barrier coating materials,” *Surf. Coatings Technol.*, vol. 202, no. 4–7, pp. 688–692, Dec. 2007.

[23] S. Gutzov and W. Assmus, “The luminescence of holmium doped cubic yttria-stabilized zirconia,” vol. 9, pp. 275–277, 2000.

[24] L. Riseberg and H. Moos, “Multiphonon orbit-lattice relaxation of excited states of rare-earth ions in crystals,” *Phys. Rev.*, vol. 174, no. 2, 1968.

[25] R. P. Ingel and D. L. Iii, “Lattice Parameters and Density for Y203-Stabilized,” no. April, pp. 27–29, 1986.

[26] P. Manning, J. Sirman, R. De Souza, and J. Kilner, “The kinetics of oxygen transport in 9.5 mol% single crystal yttria stabilised zirconia,” *Solid State Ionics*, vol. 100, pp. 1–10, 1997.

[27] V. B. Vykhodets, T. E. Kurennykh, a. G. Kesarev, M. V. Kuznetsov, V. V. Kondrat’ev, C. Hülsen, and U. Koester, “Diffusion of insoluble carbon in zirconium oxides,” *JETP Lett.*, vol. 93, no. 1, pp. 5–9, Mar. 2011.

[28] M. Kilo, M. a. Taylor, C. Argirusis, G. Borchardt, B. Lesage, S. Weber, S. Scherrer, H. Scherrer, M. Schroeder, and M. Martin, “Cation self-diffusion of [sup 44]Ca, [sup 88]Y, and [sup 96]Zr in single-crystalline calcia- and yttria-doped zirconia,” *J. Appl. Phys.*, vol. 94, no. 12, p. 7547, 2003.

[29] Y. Kodera, C. L. Hardin, and J. E. Garay, “Transmitting, emitting and controlling light: Processing of transparent ceramics using current activated pressure assisted densification,” *Scr. Mater.*, Feb. 2013.

[30] G. Dieke, *Spectra and Energy Levels of Rare Earth Ions in Crystals*. John Wiley & Sons Inc., 1968.

[31] C. Hardin, Y. Kodera, S. Basun, D. Evand, and J. E. Garay, “Transparent, luminescent terbium doped zirconia: development of optical-structural ceramics with integrated temperature measurement functionalities,” *Opt. Mater. ...*, vol. 39, pp. 1264–1269, 2013.

[32] R. C. Garvie and P. S. Nicholson, “Phase Analysis in Zirconia Systems,” no. June, pp. 303–305, 1972.

[33] D. R. Clarke and F. Adar, “Measurement of the Crystallographically Transformed Zone Produced by Fracture in Ceramics Containing Tetragonal Zirconia,” *J. Am. Ceram. Soc.*, vol. 65, no. 6, pp. 284–288, Jun. 1982.

[34] F. Yang, X. Zhao, and P. Xiao, “In Situ Measurement of Stresses and Phase Compositions of the Zirconia Scale During Oxidation of Zirconium by Raman Spectroscopy,” *Oxid. Met.*, vol. 81, no. 3–4, pp. 331–343, Aug. 2013.